

Tracking down the ENSO delayed oscillator with an adjoint OGCM

Geert Jan van Oldenborgh, Gerrit Burgers

KNMI, De Bilt, The Netherlands

Stephan Venzke, Christian Eckert

Max-Planck-Institut für Meteorologie, Hamburg, Germany

Ralf Giering

Massachusetts Institute of Technology, Cambridge, USA

August 1997

Abstract

The adjoint of an ocean general circulation model is used as a tool for investigating the causes of changes in ENSO SST indices. We identify adjoint Kelvin and Rossby waves in the sensitivities to sea level and wind stress at earlier times, which can be traced back for more than a year through western and weak eastern boundary reflections. Depending on the thermocline depth the first and second baroclinic modes are excited. The sensitivities to the heat flux and SST are local and decay in about a month.

The sensitivities to the fluxes are converted into the influence of SST using the adjoint of a statistical atmosphere model. Focusing on SST perturbations in the index region itself, we recover, up to a scale factor, the delayed oscillator concept.

submitted to Monthly Weather Review

1 Introduction

The first description of many components of ENSO was given by Walker (1923,1924). Bjerknes (1966) gave a physical mechanism that identified a positive feedback loop. The next goal was the identification of the mechanisms behind the oscillations, *i.e.*, the negative feedback that ends a warm (or cold) episode, and if possible, to predict the changes 3–12 months ahead of time. The last decade yielded much improved data from the TOGA-TAO experiment and remote sensing, and modelling capabilities have increased steadily.

These models span the range from a stochastically forced harmonic oscillator (Burgers, 1997) and canonical correlation analyses (Barnston and Ropelewski, 1992) to coupled shallow-water models (e.g., Zebiak and Cane, 1987; Schopf and Suarez, 1988; Kleeman et al., 1995) and general circulation models (Ji et al., 1996; Barnett et al., 1993). Several hypotheses for the mechanisms that are important in the observed ENSO signal have been proposed, and identified in relatively simple ocean-atmosphere models that give rise to ENSO-like oscillations but can still be analysed analytically.

The standard paradigm of ENSO oscillations describe the phenomenon as a delayed oscillator (Suarez and Schopf, 1988; Battisti and Hirst, 1989). Consider SST anomalies in the eastern equatorial Pacific. On short time scales a positive anomaly will weaken the temperature difference with the western Pacific, and hence weaken the trade winds, which in turn diminishes the amount of upwelling. The subsiding trade winds also generate Kelvin waves that propagate to the east and deepen the thermocline there, levelling off the wind-generated slope. Both effects lead to even higher temperatures. This classical positive feedback mechanism (Bjerknes, 1966) is kept in check by non-linear effects and by the effect of an accompanying equatorial Rossby wave, which reflects off the western coasts as a negative anomaly Kelvin wave and hence gives a negative feedback some time δ later. The delayed oscillator contains these three effects as

$$\frac{dT}{dt} = aT - bT^3 - cT(t - \delta) , \quad (1)$$

with T some index of the SST in the eastern Pacific, and $a, b, c, \delta > 0$. The T^3 term does not influence the period very much, but is the simplest way to represent non-linear effects that keep the oscillations bounded.

This relation has been diagnosed in many models of the tropical Pacific, and gives rise to oscillations with time scales comparable with the observed ENSO record. Evidence for a version of this mechanism is present in nature has been presented by Mantua and Battisti (1994); Kessler and McPhaden (1995).

However, many other possible modes have been proposed to be active in ENSO oscillations. The waves of the delayed oscillator can be summed in a fast-wave limit to an effective change in thermocline depth, leading to a ‘recharge’ formulation (Wyrski, 1975; Jin, 1997). On the other hand, the ‘SST slow mode’ (Neelin, 1991) is a coupled ocean-atmosphere mode related to the anomalous precipitation patterns of El-Niño events. Also, atmospheric events (westerly wind-burst, Madden-Julian oscillations) may be responsible for driving ENSO oscillations (?). All these fall outside the scope of this article, which focuses on the role of the ocean.

In this study we try to identify the delayed oscillator mechanism operating in an ocean general circulation model. The approach we take is based on the observation that most indicators for ENSO are highly correlated (which, incidentally, frustrates the search for a second independent variable to set up an oscillator). Most effects can therefore be related to a single function, say the NINO3 index of sea surface temperature in the eastern Pacific, and we rephrase the question to the cause of ENSO as the computation of the sensitivity of this index to changes in the forcing fields or state of the ocean at earlier times. For small deviations this question can be addressed with an adjoint model, which can trace all influences on one scalar function back in time.

We describe the HOPE OGCM in section 2, together with a statistical atmosphere model that is used in some experiments. This ocean model describes ENSO reasonably well (section 2.3). In section 3 we describe the adjoint ocean model. Using this we search for the sensitivity of a NINO index to forcing fields (heat flux, wind stress) and state variables (sea level height, temperature) in section 4. With the help of the adjoint statistical atmosphere model we transform the sensitivities to fluxes into sensitivities to SST anomalies, which are then simplified into a description resembling the delayed oscillator in section 5. Our conclusions are presented in section 6. Two appendices contain technical details and validation runs of the adjoint model.

2 Model Description

2.1 The ocean model

The ocean model used in this study is HOPE (The Hamburg Ocean Primitive Equation Model, Wolff et al., 1997). As we are mainly interested in ENSO we use a domain that is limited to the Pacific Ocean (120°E–70°W, 55°S–67°N). The model has a 2.8° resolution, with the meridional resolution gradually

increased to 0.5° within the region 10°N to 10°S . There are 20 vertical levels which are irregularly spaced in such a fashion that ten levels are placed in the upper 300 meters. The model contains a realistic bottom topography. The numerical scheme uses the Arakawa E-grid (Arakawa and Lamb, 1977) and a two-hour time step. We use a 360-day year subdivided in 12 equal-length months of 4 weeks each. There is no diurnal cycle.

A Newtonian relaxation is employed to restore the surface salinity within the whole domain to the climatology of Levitus (1982) using a time constant of 40 days. Otherwise, no explicit fresh water flux is provided. Prognostic variables are the three-dimensional fields of horizontal velocity, temperature and salinity, and the sea surface elevation. Physical parametrizations in HOPE include solar penetration below the surface. About 14% of the solar radiation incident on the ocean surface is allowed to penetrate beneath the 20 m surface layer of the model (Paulson and Simpson, 1977; Schneider et al., 1996). The vertical mixing in HOPE is based on a Richardson-number dependent formulation and a simple mixed layer scheme to represent the effects of wind stirring (see Latif et al. (1994) for details). Further details about the model physics as well as the numerical scheme are given in the HOPE documentation (Wolff et al., 1997).

2.2 The atmosphere model

For most experiments in this paper we used prescribed heat flux and wind stress fields. These were generated with the ECHAM-3 atmosphere from observed SST fields and stored as daily values. ECHAM-3 is the Hamburg version of the European Centre operational weather forecasting model. It is described in detail in two reports (Roeckner et al., 1992; DKRZ, 1992). The SSTs were taken from a data set of the British Meteorological Office (UKMO), which is referred to as the ‘GISST’ data set (Parker et al., 1994). Additionally, we imposed a relaxation to observed SSTs of $40 \text{ Wm}^{-2}/\text{K}$, using a Newtonian formulation. This is required to compensate for model drift, which produces systematic differences of the simulated SSTs compared to the observed ones that were used to generate the atmospheric forcing with the ECHAM-3 model.

A statistical atmosphere model similar to the one used by Barnett et al. (1993) is used to convert the sensitivities of the ocean model to these fluxes into sensitivities to SST. This simple atmosphere model is essentially a regression relationship: wind stress anomalies and surface heat flux anomalies are related to sea surface temperature anomalies. This dependence is almost instantaneous and non-local. It reproduces the large-scale response of the atmosphere to large-scale SST anomalies. In particular, the Bjerknes

positive feedback of reduced trade winds resulting from a reduced east-west SST gradient is well-reproduced in this type of model. On the other hand, smaller-scale atmospheric responses, such as the SST slow mode, are not caught.

The regression matrix is derived from an integration of the atmospheric general circulation model ECHAM-3 with prescribed observed global SSTs during the period 1949 to 1990. The linear regression is done in an Empirical Orthogonal Function space, retaining the first 10 EOFs of the anomalies, which account for 63% and 49% of the field variance in the SST and the atmospheric fields, respectively. The dominant modes of interannual variability are found to be well captured by the EOF truncation. To compensate for systematic deficiencies of the OGCM, its simulated SST anomaly is corrected using another regression matrix based on the leading 10 EOFs of observed and simulated SST anomaly. The latter are obtained by forcing the ocean model by the wind stresses and surface heat fluxes from the ECHAM-3 integration mentioned above.

Let the observed and simulated SST anomalies be denoted by $T_{\text{obs}}(x, t)$ and $T_{\text{sim}}(x, t)$, respectively. The zonal and meridional wind stress anomalies were pooled together with the surface heat flux anomalies in one data set of atmospheric flux anomalies denoted by $\mathcal{F}_{\text{echam}}(x, t)$. The EOF expansions of the observed and simulated fields are

$$T_{\text{obs}}(x, t) = \sum_n \alpha_n(t) e_n(x) \quad (2)$$

$$\mathcal{F}_{\text{echam}}(x, t) = \sum_m \beta_m(t) f_m(x) \quad (3)$$

$$T_{\text{sim}}(x, t) = \sum_l \gamma_l(t) g_l(x) . \quad (4)$$

The linear regressions yield matrices $C^{(1)}$ and $C^{(2)}$ whose entries are given by

$$C_{mn}^{(1)} = \frac{\langle \beta_m \alpha_n \rangle}{\langle \alpha_n^2 \rangle} \quad (5)$$

$$C_{nl}^{(2)} = \frac{\langle \alpha_n \gamma_l \rangle}{\langle \gamma_l^2 \rangle} . \quad (6)$$

Angle brackets signify time averages. The estimated wind stress anomaly, $\mathcal{F}_{\text{est}}(x, t)$, may now be obtained by the simulated SST anomaly via

$$\mathcal{F}_{\text{est}}(x, t) = \sum_m \beta_{\text{est},m}(t) f_m(x) , \quad (7)$$

with

$$\beta_{\text{est},m}(t) = \sum_{n,l} C_{mn}^{(1)} C_{nl}^{(2)} \gamma_l(t) . \quad (8)$$

To compensate again for systematic differences between the observed SSTs for which the surface heat fluxes have been computed by ECHAM-3 and the SSTs that are actually simulated by the HOPE model, the matrix $C^{(2)}$ is employed again. The additional surface heat flux correction is given by

$$Q_{\text{cor}}(x, t) = \lambda(T_{\text{sim}}(x, t) - T_{\text{obs,est}}(x, t)) \quad (9)$$

$$T_{\text{obs,est}}(x, t) = \sum_n \sum_l C_{nl}^{(2)} \gamma_l(t) e_n(x) , \quad (10)$$

with the relaxation constant $\lambda = -10 \text{ Wm}^{-2}/\text{K}$. As the estimates for the wind stress and surface heat flux anomalies are always made for the next month to be integrated, the linear regressions are computed with the SSTs leading the atmospheric fields by one month.

2.3 ENSO simulated by HOPE

Next we establish whether the model used is in fact able to reproduce the observed behaviour of ENSO. The ocean model was spun up from the Levitus climatology for 30 years with climatological forcing. It was then integrated for 42 years starting in January 1949, using wind stress and surface heat fluxes from the ECHAM-3 atmosphere model integration described in section 2.2 as upper boundary conditions, including the 40 Wm^{-2} relaxation to observed SST.

The spatial structure as well as the temporal evolution of observed and simulated interannual SST anomalies in the Pacific Ocean can be inferred from the pattern of the first EOF and the associated principal component shown in Fig. 2. Overall, the anomaly structure is simulated reasonably well by the HOPE model. There are, however, some differences to the observations. The simulated SST anomalies are too much equatorially confined, and they extend too far into the western Pacific. The latter deficiency is related to the too strong cold tongue which extends too far into the western Pacific. Hence, in addition to the average SST in the NINO3 region (5°S – 5°N , 90°W – 150°W) we will use a slightly further western region (NINO3.4: 5°S – 5°N , 120°W – 170°W) as an ENSO index in our sensitivity studies. The comparison of the principal components reveals satisfactory agreement ($r = 0.88$) between the temporal evolution of the simulated and observed SST anomalies.

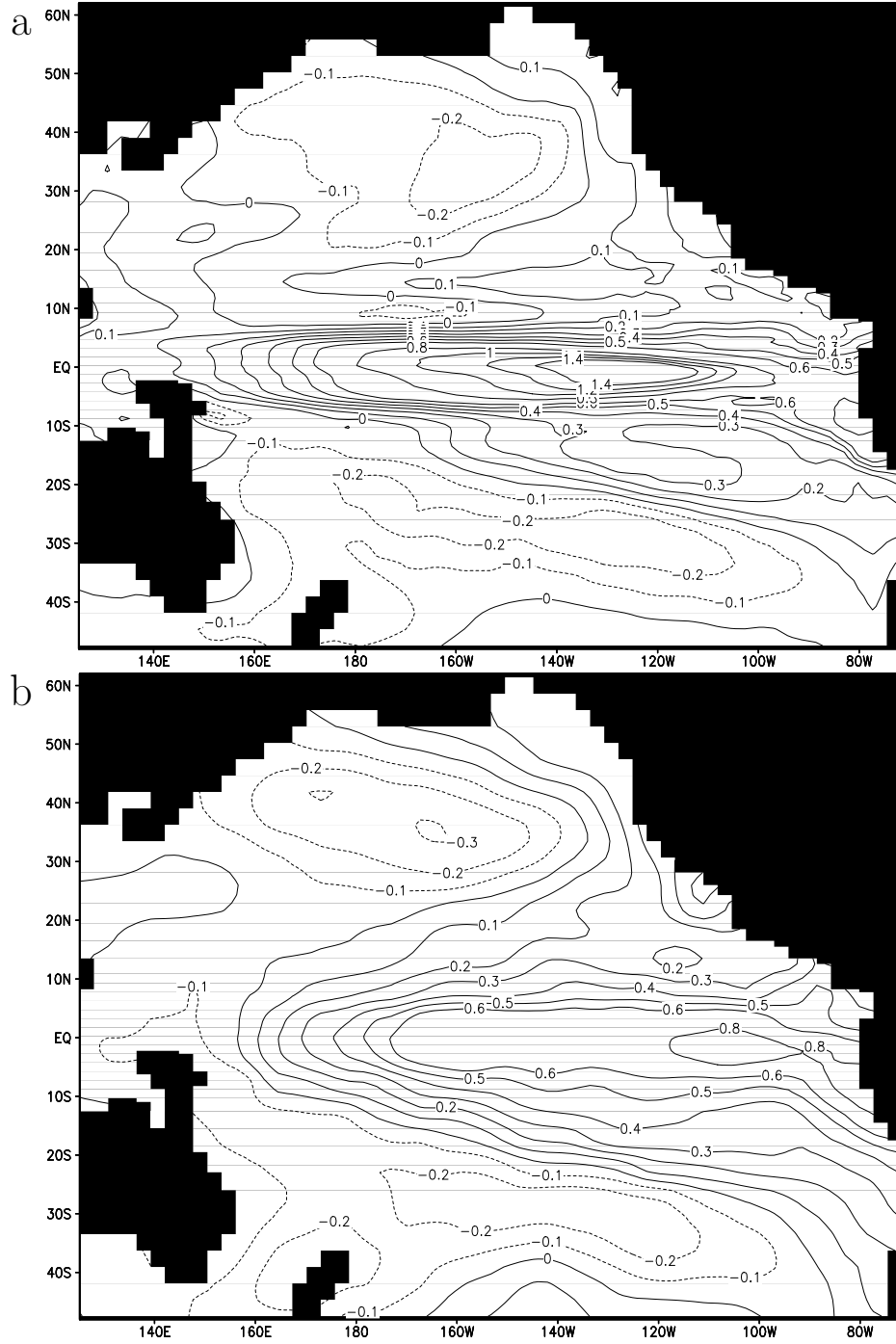


Figure 1: Maps of the first EOF of monthly mean SST anomalies from 1949 to 1990 as derived from (a) the HOPE model simulation and (b) observations (GISST data set) explaining 26% and 29% of the total variance, respectively.

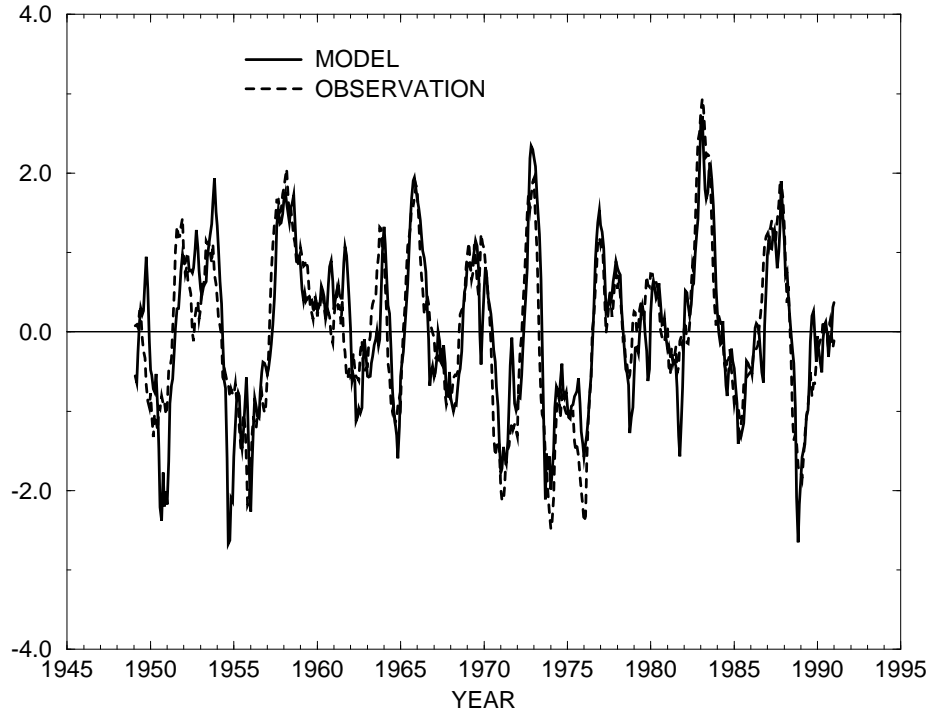


Figure 2: Time series of the principal components.

The HOPE model can be coupled to the statistical atmosphere described in the previous section instead of being forced by prescribed upper boundary conditions. Such a combination of an OGCM and a statistical atmosphere model is generally referred to as a Hybrid Coupled Model (HCM). It shows a regular oscillation of the SST anomalies with a period of 2.5 years. The spatial structure and amplitude of the SST anomalies are comparable to those obtained with prescribed forcing (Fig. 1a).

3 The adjoint model

In this section we define what we mean by the term ‘adjoint model’ and present some aspects of the adjoint of the OGCM we constructed.

3.1 Definition

The system being studied is described by a state vector x of prognostic variables. Let the model \mathcal{M} be some function, in general non-linear, that computes from an initial state x_0 and a set of forcing fields y_i at times

t_i ($i = 1, \dots, n$) a state vector x_n at time t_n

$$x_n = \mathcal{M}(x_0, y_i) . \quad (11)$$

The tangent model $M(x_0, y_i)$ is the linear mapping that gives the effect on x_n of infinitesimal changes in the initial state δx_0 and in the set of forcing fields δy_i

$$\delta x_n = M(x_0, y_i) \begin{pmatrix} \delta x_0 \\ \delta y_i \end{pmatrix} = \lim_{\epsilon \rightarrow 0} \frac{\mathcal{M}(x_0 + \epsilon \delta x_0, y_i + \epsilon \delta y_i) - \mathcal{M}(x_0, y_i)}{\epsilon} . \quad (12)$$

Let $f(x_n)$ be some scalar function of the final state, for instance an averaged field, index or cost function. We can now compute the change in this function of the final state as a result of a change in the initial state and forcing fields as

$$\begin{aligned} \delta f(x_n) &= \frac{\partial f(x_n)}{\partial x_n} \delta x_n = \frac{\partial f(x_n)}{\partial x_n} M(x_0, y_i) \begin{pmatrix} \delta x_0 \\ \delta y_i \end{pmatrix} \\ &= (\delta x_0, \delta y_i) M^\dagger(x_0, y_i) \frac{\partial f(x_n)}{\partial x_n} = (\delta x_0, \delta y_i) \begin{pmatrix} \partial f(x_n)/\partial x_0 \\ \partial f(x_n)/\partial y_i \end{pmatrix} , \end{aligned} \quad (13)$$

with the mapping $M^\dagger(x_0, y_i)$ the adjoint model. It propagates the sensitivities of the scalar f to the final state back to the initial state, and can be seen as a backward derivative of the model.

In practice, the model \mathcal{M} consists of a series of discrete time steps $x_i \rightarrow x_{i+1}(x_i, y_i)$ for $i = 0, \dots, n-1$, so

$$\begin{aligned} x_n &= x_n(x_{n-1}, y_{n-1}) \\ &= x_n(x_{n-1}(x_{n-2}, y_{n-2}), y_{n-1}) \\ &= \dots \end{aligned} \quad (14)$$

The adjoint model is then evaluated by time-stepping the discrete model back from t_n to t_0 , at each step applying the chain rule of differentiation with respect to the model variables

$$\frac{\partial f(x_n)}{\partial x_i} = \frac{\partial f(x_n)}{\partial x_{i+1}} \frac{\partial x_{i+1}}{\partial x_i} \quad (15)$$

and the forcing fields

$$\frac{\partial f(x_n)}{\partial y_i} = \frac{\partial f(x_n)}{\partial x_{i+1}} \frac{\partial x_{i+1}}{\partial y_i} . \quad (16)$$

Note that the evolution of the adjoint fields $\partial f/\partial x_i$ does not depend on the function f , hence except for the initialization of $\partial f/\partial x_n$ the adjoint model is independent of the function f . Physically, the adjoint field represents the sensitivity of f to infinitesimal perturbations of the prior state x_i and forcing field y_i . For a non-linear model \mathcal{M} , the response to a finite perturbation may or may not be similar. An example of the latter case is convection, which is often represented by a step function of the difference in density of two layers. The derivative of this function to the density is zero almost everywhere, yet a finite perturbation can induce or inhibit convection.

The two types of adjoint fields in Eqs (15) and (16) are conceptually different. Derivatives to forcing fields $\partial f/\partial y_i$ (for instance externally prescribed fluxes) are not used at times $t < t_i$. These adjoint fields thus represent quantities that can be varied independently. On the other hand, derivatives to internal model state fields $\partial f/\partial x_i$ are used in the previous time step to compute $\partial f/\partial x_{i-1}$, and hence cannot explicitly be varied without invalidating the adjoint model for $t < t_i$.

As defined above the adjoint field is an extensive variable: the influence of a single grid box is proportional to its size. Also, the influence is proportional to the time step used. We therefore normalize the adjoint field to the grid box size and a time interval of one day and give the derivative to forcing fields (fluxes) in units $[f]/([x] \text{ day sr})$.

3.2 Adjoint HOPE and atmosphere models

We constructed adjoint models (as defined above) of the ocean and atmosphere models in the following way.

In HOPE, a time step consists of a cycle of separate tasks (split operators). For each of these subroutines (or easily definable subdivisions) the adjoint code was generated using the Adjoint Model Compiler (Giering and Kaminski, 1996; Giering, 1994). This tool gives computer code which is the adjoint of the original algorithm. This code was hand-optimized in some algorithms where there is a simpler formulation (the inversion of tridiagonal matrices). These adjoint subroutines were then integrated into an adjoint model. Further details can be found in Appendix A.

This construction gives the exact adjoint of the complete (discrete) model. We realize that there are many partial derivatives that can probably be safely neglected, like the dependence of the mixing parameters on the temperature and the detailed intricacies of the equation of state. However, it is a nontrivial task to verify that omissions are in fact harmless, and we did not (yet) perform this analysis.

There is one point where it was necessary to deviate from the exact derivatives to include some non-linear effects. In our model the vertical eddy viscosity A_V and diffusivity D_V depend on the Richardson number R as

$$A_V = \frac{A_{V,0}}{(1 + C_A R')^2} + \text{other terms} \quad (17)$$

$$D_V = \frac{D_{V,0}}{(1 + C_D R')^3} + \text{other terms} \quad (18)$$

$$R = \frac{-g\partial\rho/\partial z}{(\partial u/\partial z)^2 + (\partial v/\partial z)^2} \quad (19)$$

$$R' = \max(0, R) \quad (20)$$

with $C_A = C_D = 5$. For marginally stable layers ($0 < R < R_{\text{cut}} = 0.3$) the large derivatives $\partial A_V/\partial R$, $\partial D_V/\partial R$ are not very good estimates for the effect of a finite perturbation, as the functions have very sharp kinks at $R = 0$. In practice this manifests itself as dipoles of very strong positive and negative influence one vertical grid point apart in the adjoint temperature and salinity fields. This instability can be suppressed by smoothing the derivatives of Eqs (17–18). In the evaluation of the derivative, we therefore use $R' = R_{\text{cut}}^2/R$ for $0 < R < R_{\text{cut}}$.

The adjoint of the statistical atmosphere model was constructed in a similar fashion. As this is a linear model, it does not depend on the forward fields, which simplifies the code. The time lag between the SST and fluxes that the atmosphere model introduces has been taken into account.

4 Sensitivity experiments

To investigate the causes of temperature changes in the eastern tropical Pacific in the HOPE model we performed a few experiments with the adjoint HOPE model described in section 3.2 using prescribed fluxes. These experiments are the exact opposite of perturbation experiments that search for all effects of one given perturbation, usually a wind burst (e.g., Giese and Harrison, 1990). We search backwards in time to find all sensitivities of one target function, which we take to be the NINO3 (or NINO3.4) index of SST in the eastern Pacific. A sensitivity field gives the change in the target function if we would have added a perturbation at that time and place.

From perturbation studies and lag-correlation analyses (Gill, 1982; Philander, 1990) it has been found that many perturbations propagate as equatorial Kelvin or Rossby waves. The baroclinic Kelvin waves travel eastwards within a few degrees of the equator, with a speed of 2–3 ms⁻¹. The

n -th mode Rossby waves travel to the west at $1/(2n + 1)$ times this speed, with a maximum perturbation to the sea level for the first three modes at about 5° , $8\text{--}10^\circ$ and $12\text{--}15^\circ$ off the equator (in theory, these are $\sqrt{3/2}$, $\sqrt{3}$ and $\sqrt{(5 + \sqrt{18})/2}$ Rossby radii). This propagation implies that sensitivities propagate backwards along the same trajectories, which we refer to as adjoint Kelvin or Rossby waves. We will verify this interpretation by checking that the propagation speed is consistent with predictions from linear theory.

As background for the sensitivity experiments we used the years 1987 and 1988. In 1987 there was an El-Niño episode (the observed NINO3 index was $+1.5\text{ K}$ to $+2.0\text{ K}$ for much of the year, but had returned to 1.0 K by the end of December), whereas 1988 ended on a strong cold anomaly (-1.5 K). As target dates we took October 1987 (warm), December 1987 (transition) and December 1988 (cold). We studied the sensitivity of the NINO3 index N_3 (NINO3.4 index $N_{3.4}$) at these times to various fields at earlier times. The interesting ones are the input fluxes (wind stress $\tau_{x,y}$ and the heat flux Q) and state variable sea level height ζ . The former have been averaged over 7.5 day ‘weeks’, the latter is sampled at the beginning of these periods¹. Unless otherwise noticed the illustrations are from the run to December 1987.

4.1 Sea level

The clearest signals can be seen in the sensitivity to the sea level. This is due to the fact that, as in the forward case, the adjoint Kelvin and Rossby waves are clearly separated by latitude. In the eastern Pacific, temperature and sea level are very strongly correlated. A higher sea level indicates a deeper thermocline, which in turn causes the sea surface to be less cold. It is therefore no surprise to see that at the end of December 1987, just before the target date, the NINO3 index would have been higher if the sea level would have been higher in the same area. The NINO3 index is the average temperature in the middle box shown in Fig. 3a. The sensitivity is thus positive and confined to this region, with an emphasis on the upwelling region. (The slightly negative field in the western Pacific is a weak barotropic mode.)

Going back in time, at the beginning of November (Fig. 3b), one can see an adjoint Kelvin wave coming from the western Pacific, and some adjoint $n = 1$ Rossby waves coming from the eastern boundary. The adjoint Kelvin wave should be interpreted as follows: *if* the sea level would have been infinitesimally higher in the stippled area in November 1987, then there would

¹MPEG movies and space-time diagrams of the experiments are available at <http://www.knmi.nl/~oldenbor/Sense/pictures.html>.

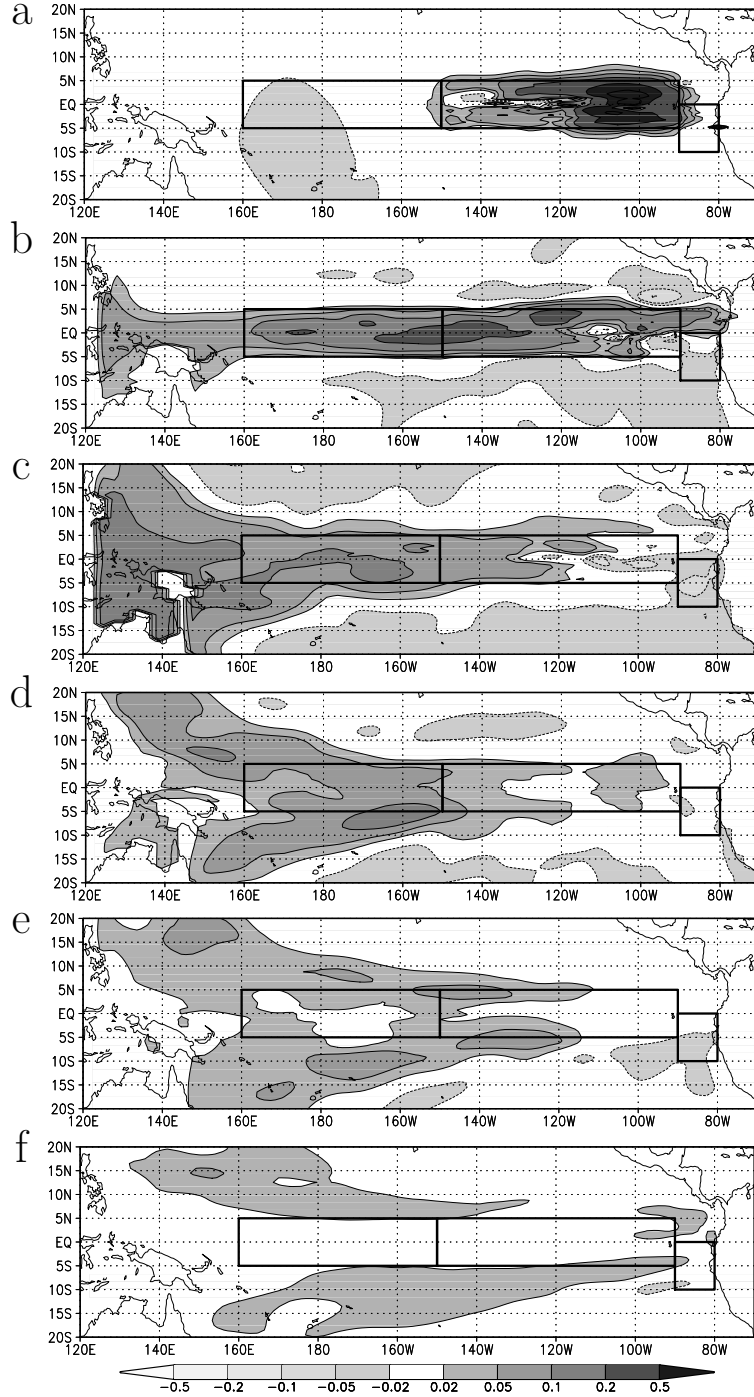


Figure 3: The sensitivity of the NINO3 index to sea level changes $\partial N_3 / \partial \zeta$ in K/m/sr at the end of 1987 in the last week of December (a), the first weeks of November (b), July (c), April (d) and January 1987 (e), and July 1986 (f). The boxes denote, from east to west, the NINO12, NINO3 and NINO4 index regions.

have been a baroclinic Kelvin wave added to the actual state at the position indicated, and the temperature would have been infinitesimally higher in the NINO3 area 2 months later. The Kelvin wave would have depressed the thermocline in that region.

In the beginning of July (Fig. 3c), all the adjoint Rossby waves going to the measurement region from the eastern boundary have reached the coast. These are partially reflected and on the way back as the tail of the direct adjoint Kelvin wave. The resolution does not permit coastal Kelvin waves to travel north and south. On the other side, the adjoint equatorial Kelvin wave has reflected at the western coasts into a set of adjoint Rossby waves. The first blob at 165°W corresponds to the $n = 1$ reflection off New Guinea, the second one (at 150°E) has been reflected off the Philippines. (The HOPE land-sea mask has approximately two north-south walls at these locations.) At the same longitude the $n = 2$ reflection off New Guinea is forming, and further west the beginnings of higher-order adjoint Rossby waves can be discerned. The presence of the parity-odd $n = 2$ mode is due to the fact that the western coast has some structure in our model.

Three months earlier (Fig. 3d) the first adjoint Rossby wave has almost dissipated, the strongest signal is now at 160°W . The southern $n = 2$ signal is now at the dateline, whereas the northern reflection has reached 150°E , clearly separated from the $n = 3$ reflection. The situation at the beginning of January is not much different (Fig. 3e).

At the beginning of July 1986, 18 months before the NINO3 index is evaluated (Fig. 3f), the only influence remaining is a pattern of higher order Rossby waves that slowly traverses the basin. This sensitivity on the sea level, and equivalently the thermocline depth, of the off-equatorial warm pool is in agreement with the original recharge hypothesis (Wyrtki, 1975). However, a sensitivity of the NINO indices to the zonally-averaged thermocline depth along the equator at this time scale (Jin, 1997) is not seen.

The reflection pattern off the western coasts is clearly visible in the space-time diagrams of 5° latitude bands at 5°N , the equator and 5°S in Fig. 4. In 1987, the adjoint Kelvin wave, travelling at about 2ms^{-1} (dashed line in Fig. 4b) reaches the coast of New Guinea in the first week of October, generating a Rossby wave at 5°S that picks up a Northern component some time later. The main reflection at 120°E occurs at the end of September.

The demise of the first adjoint Rossby wave at the edge of the warm pool seems to give rise to a second adjoint Kelvin wave travelling back to the western boundary. At the same time the Kelvin wave reflected at the east coast arrives, especially in the 1988 experiment with strong adjoint $n = 1$ Rossby waves in the eastern Pacific. This Kelvin wave is reinforced by the energy reflected off the western coast of New Guinea by the Rossby wave

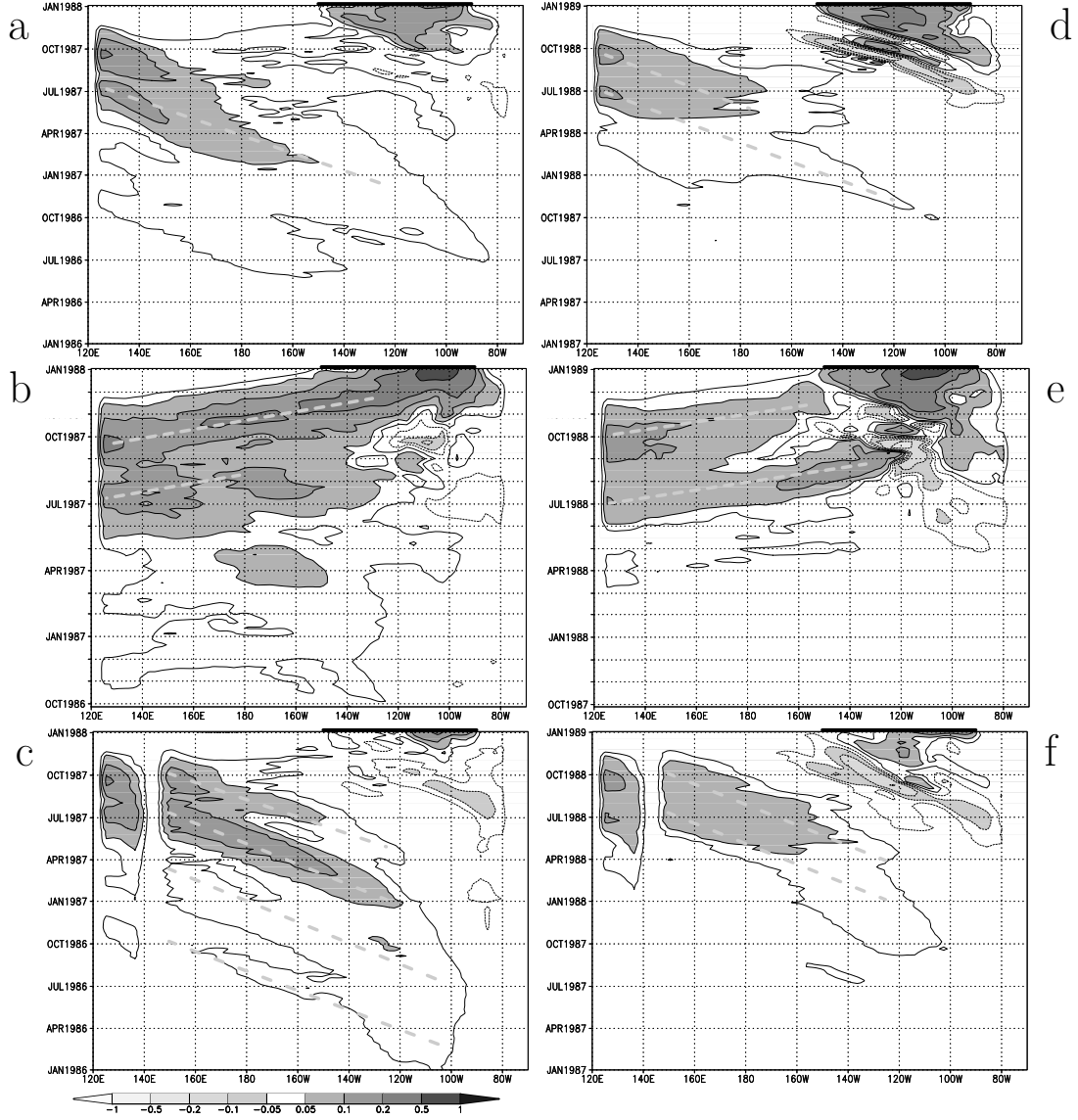


Figure 4: The sensitivity of the NINO3 index to sea level changes in December 1987 $\partial N_3 / \partial \zeta$ in K/m/sr at 5°N (a), the equator (b) and 5°S (c), averaged over 5° latitude bands; the same one year later, to December 1988 (d,e,f).

reflected off the Philippines. Halfway July this generates a third adjoint Rossby wave. This western mechanism seems to produce a fourth and fifth Rossby wave in February 1987 and November 1986 respectively.

These reflected Rossby waves merge into a structure with an effective group velocity that is significantly lower than the phase velocity of the individual $n = 1$ Rossby waves, indicated by the dashed lines in Fig. 4a,c with speed 0.6 ms^{-1} . This behaviour is very similar to the properties of the observed Kelvin and Rossby waves that constitute ENSO oscillations (Chao and Philander, 1993; ?).

In 1987, there are also adjoint Rossby waves with opposite sign east of 150°W . They are generated by the adjoint Kelvin wave leaving the NINO3 signal region and reach the eastern coast within a few months. These waves are much stronger in 1988, in cold conditions. The adjoint Kelvin wave is faster and weaker, and a second Kelvin wave is now clearly generated by the Rossby wave activity reflecting off the east coast. In HOPE the NINO3 region is characterized by intense currents and changes in thermocline depth at this time, so that linear theory is not applicable. The reflected adjoint Rossby waves seem to have the same speed as in 1987, but are again weaker.

These reflection patterns are compatible with observations from sea level measurements near the eastern and western boundaries (Boulanger and Fu, 1996). Some of the discrepancies at the western coast reported in this paper may be explained by the multiple reflections observed in our model.

4.2 Wave speeds

To check the interpretation of Kelvin and Rossby waves, we have measured the speeds of the structures visible in the adjoint run and compared the results to wave speeds calculated from the density structure of the model.

The speed was estimated by taking 1- and 2-month lag correlations for each latitude. From Fig. 5 one can read off the following speeds for the waves. In the last month of the run leading to the NINO3 index at the end of December 1987, the equatorial Kelvin wave has a speed that varies between 1.8 ms^{-1} at 1°S , 2.0 ms^{-1} on the equator and 2.4 ms^{-1} at 2°N (Fig. 5a). In the experiment leading to October 1987 we find speeds of 2.1 to 2.9 ms^{-1} (Fig. 5b), and at the end of 1988 they are just over 3 ms^{-1} (Fig. 5c).

The Rossby waves during these times in the Eastern Pacific have speeds at 5°N of 0.5 ms^{-1} , 0.4 ms^{-1} and 0.8 ms^{-1} , this is somewhat slower than $1/3$ the speed of the Kelvin waves due to the shallower thermocline. The speeds of reflected adjoint Rossby waves in the central Pacific have been read off Fig. 5d. The northern branches of the Rossby waves move with -0.55 ms^{-1} (5°N), -0.34 ms^{-1} (10°N) and -0.16 ms^{-1} (17°N). The southern lobes are

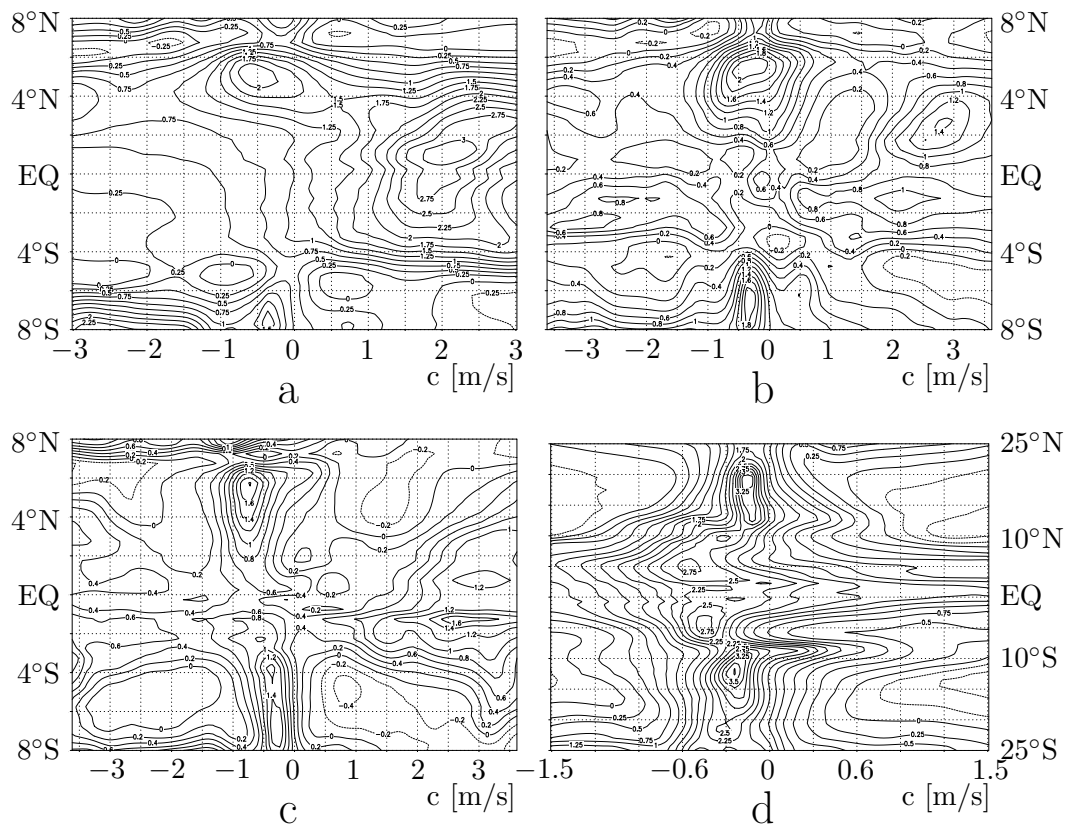


Figure 5: The 1-month lag correlation in m/s of $\partial N_3/\partial \zeta$ in the last month of the Dec 1987 run (a), the Oct 1987 run (b), the Dec 1988 run (c), and the 2-month lag correlation in January–April 1987 (d). The contours refer to $-\log(1-p)$.

slower and further from the equator: -0.50 ms^{-1} (5°S), -0.22 ms^{-1} at 11°S and -0.12 ms^{-1} (19°S , only visible in 1986). These speeds are roughly the same in the other two experiments, except that the first mode is often poorly visible.

The observed adjoint Kelvin waves therefore seem to be a mixture of the first baroclinic mode, with speeds around 3 ms^{-1} , and the second baroclinic mode, with a speed of around 2 ms^{-1} . This is in agreement with other theoretical studies (e.g., Giese and Harrison, 1990). Observations of Kelvin waves give a single mode with a speed of $2.4 \pm 0.3 \text{ ms}^{-1}$ from TOGA-TAO subsurface temperatures (?) and $2.9 \pm 0.9 \text{ ms}^{-1}$ from TOPEX/POSEIDON altimetry data (Boulanger and Menkes, 1995; Chelton and Schlax, 1996). Also, in these observations the shallowing of the thermocline towards the east is compensated by a stronger density contrast across the thermocline, leading to an almost constant speed up to 110°W . In contrast, in HOPE we observe lower speeds east of 160°W (see Fig. 4), as the thermocline is not sharp enough due to discretization effects.

These speeds can also be computed from the density profiles² (see, e.g., Gill, 1982; Philander, 1990), using a rigid lid to eliminate the barotropic mode. The first three modes of the horizontal velocity are shown in Fig. 6. The first baroclinic mode has a zero around³ 1500 m and a Kelvin wave speed of $2.6\text{--}3.3 \text{ ms}^{-1}$, in agreement with the profiles discussed in Philander (1990); Giese and Harrison (1990). The next modes have their first zeroes near the thermocline, at around 100–150 m in the equatorial zone, substantially deeper elsewhere. The speed fields are shown in Fig. 7.

With a well-developed thermocline, as in the western and central Pacific, and in the east during the December 1987 run (Fig. 6a,b), a Kelvin wave in the first baroclinic mode does not influence the NINO3 index of surface temperatures as much as one in the second mode. The eigenfunction has a small amplitude at the surface, and the Richardson-number dependent mixing scheme, Eqs (17–18), effectively decouples the ocean below the thermocline. However, when the thermocline is absent in the cold tongue, as our model generates in December 1988 (Fig. 6d), the *first* mode is most effective in changing the SST in the NINO3 area, although the adjoint Kelvin wave is weaker in this case (see Figs 4b,e). The October 1987 run, with a weak thermocline, excites adjoint Kelvin waves in both modes.

²This computation depends somewhat on the mixing scheme, and is done for mixing parameters proportional to $1/N^2$, which differs from the Richardson-number based scheme with a mixed layer of the HOPE model. The difference will be mainly in the absence of a mixed layer in the computed modes.

³This mode seems to be associated with the rise in salinity around that depth in the Pacific, which is absent in the Atlantic

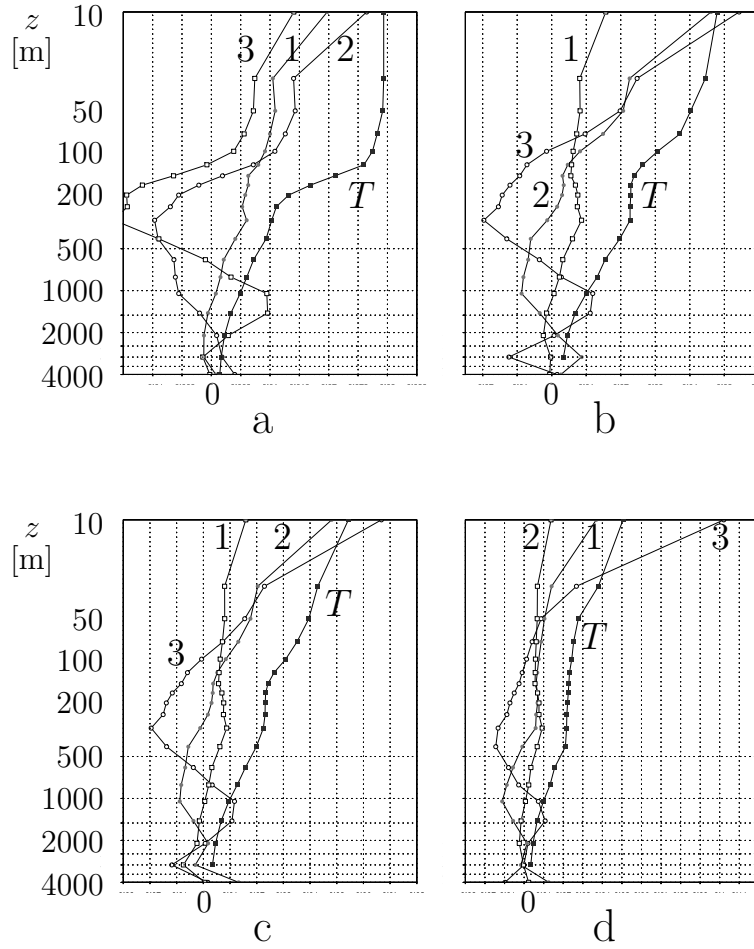


Figure 6: Profiles of the first three baroclinic modes and temperature at the equator, 180° (a) and 100°W (b) in Dec 1987, and at 100°W in Oct 1987 (c) and Dec 1988 (d) in the HOPE model.

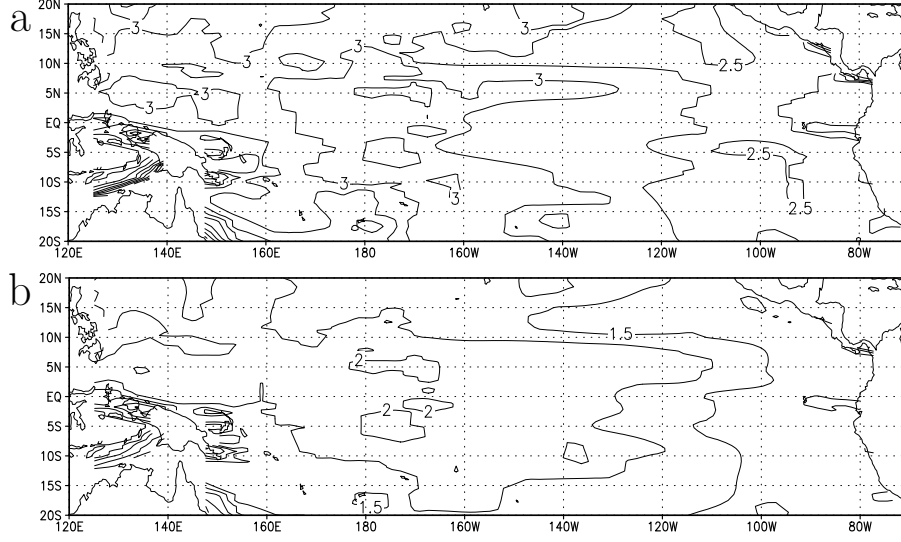


Figure 7: The speeds in ms^{-1} of the first (a) and second (b) baroclinic modes deduced from the density profiles at the end of 1987.

The speed of the second mode Kelvin wave in the December 1987 run (Fig. 5a) is slightly higher than the 1.8 to 2.1 ms^{-1} read off from the area west of the NINO3 box in Fig. 7b. In 1988 the speed corresponds well with the little over 3 ms^{-1} read off from Fig. 7a. The $n = 1$ reflected adjoint Rossby waves correspond reasonably well with $1/3$ the zonally averaged speed of the second mode (0.57 ms^{-1} at 5°S , 0.62 ms^{-1} at 5°N); the same holds for $n = 2$ ($1/5$) at 10°N (0.34 ms^{-1}) in all experiments. Note that this means that during the reflection off the western boundary energy can flow from the second into the first baroclinic mode; the WKB approximation breaks down when the depth changes significantly on scales comparable to the wavelength.

The speeds at the other extrema in Fig. 5d, corresponding to higher-order Rossby modes, are much lower and seem to resemble more the speed of the third baroclinic mode (0.21 ms^{-1} at 11°S , 0.15 ms^{-1} at 19°S and 0.17 ms^{-1} at 15°N). Unfortunately the derivatives to the horizontal speeds are too noisy to determine their vertical structure, we can only assume that the second and third modes can also be mixed up in the shallow water at the western coasts.

4.3 Wind stress

The derivative to the wind stress is a superposition of the wind fields associated with the Kelvin and Rossby waves. In Fig. 8 we show the situation

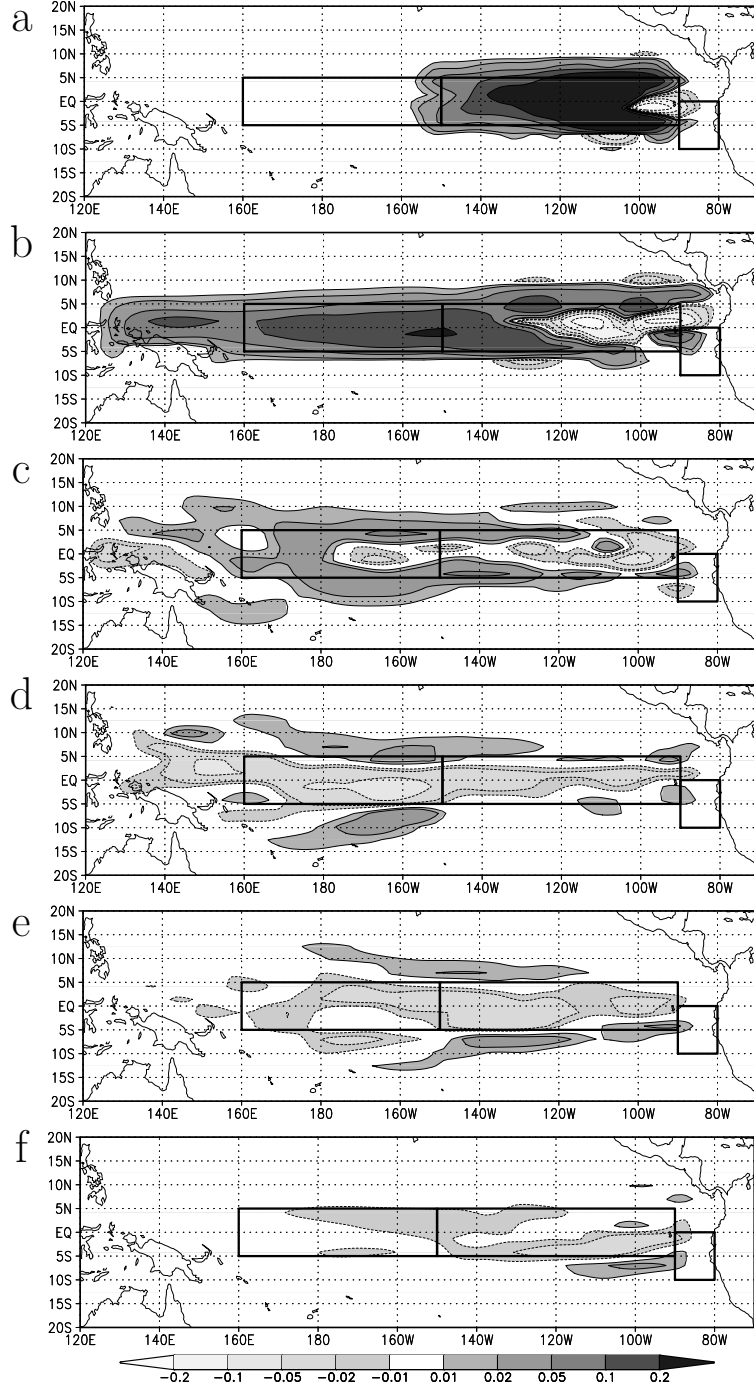


Figure 8: The sensitivity of the NINO3 index at the end of 1987 to zonal wind stress, $\partial N_3 / \partial \tau_x$ in $\text{K}/\text{Nm}^{-2}/\text{sr}/\text{day}$, at the end of 1987 (a), in the first weeks of November (b), July (c), April (d) and January 1987 (e), and July 1986 (f)

at the same times as the sensitivity to the sea level height in Fig. 3. These fields have the following interpretation: *if* there would have been a positive (eastward) anomalous wind field at the position of a positive derivative, *then* the NINO3 index would have been higher at the end of 1987.

During the first week of the adjoint run (Fig. 8a), one sees that a positive wind anomaly (weaker trade winds) reduces upwelling, and hence heats up the NINO3 region. At the extreme eastern end of the region a positive anomaly causes a more divergent wind field, and hence more upwelling and a lower NINO3 index.

At earlier times the disturbance caused by an anomalous wind field has to propagate to the eastern Pacific in order to influence this index. Comparing with the derivatives to the sea level (Fig. 3), one sees the textbook relations (e.g., Gill, 1982) that for a Kelvin wave the zonal wind field and sea level have the same shape, whereas an $n = 1$ Rossby wave has an anti-cyclonal circulation around a positive sea level anomaly. The $n = 2$ wave clearly develops its antisymmetric wind field (for instance at 160°E in Fig. 8c), whereas the $n = 3$ Rossby wave is symmetric again. However, the wind-field sensitivity of the higher order modes is much weaker than the sensitivity of the $n = 1$ mode. The 1988 experiment, during cold conditions, shows a weaker dependence on wind stress; discussion of this effect is delayed to section 5.

The result of these adjoint Kelvin and Rossby waves is that during the half year leading up to the measurement the sensitivity to τ_x at the date line is positive, meaning that a weaker easterly trade wind or even westerly wind will increase the SST at the NINO3 region. At earlier times, the sensitivity has the opposite sign — a westerly anomaly will cool the NINO3 region at these lead times.

The sensitivity to the meridional wind stress τ_y is much smaller, and just shows the edges of the structures visible in the derivative to the sea level, Fig. 3.

4.4 Heat flux

Finally, an obvious influence on the surface temperature in the NINO3 region is the heat flux into this area, or, almost equivalently, the temperature some time previously due to persistence. This is relevant only for the last few months preceding the measurement. In Fig. 9 we plot this derivative as a function of time at the equator. Except for some waves that are excited in August–September the sensitivity drops off exponentially with a time scale of about one month (25 ± 5 days). There is some advection from the north-east, but this does not extend beyond a few degrees of latitude outside the NINO3 area.

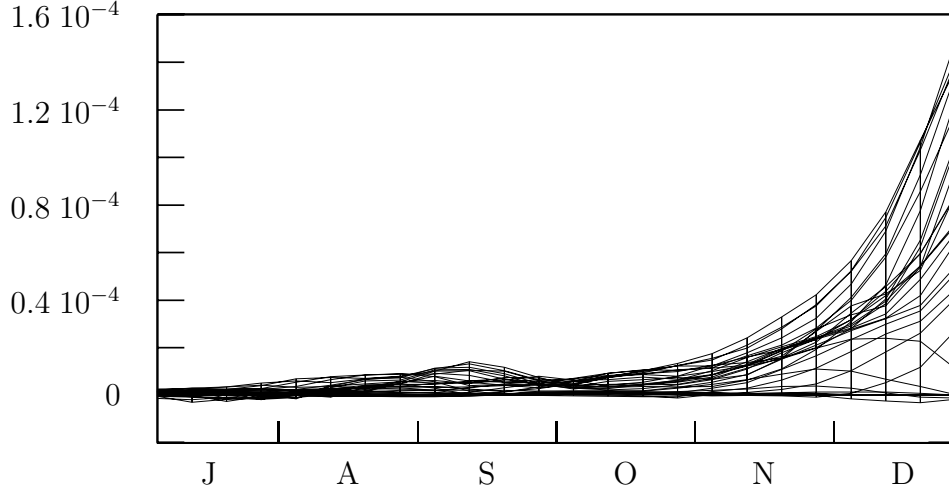


Figure 9: The sensitivity of the NINO3 index to the heat flux $\partial N_3 / \partial Q$ in $\text{K/Wm}^{-2}/\text{sr}$ for various longitudes in the eastern Pacific, averaged over 5°S to 5°N (the vertical lines connect the weekly measurements).

$n = 1$ Rossby waves are excited at the point where the thermocline is very shallow in the HOPE model (around 140°W); we assume that heat input at this point lowers the thermocline and thus excites waves; only the Rossby waves travel in the right direction to influence the NINO3 index. In other circumstances a heat flux does not efficiently excite long waves.

5 The delayed oscillator in HOPE

5.1 Outline

The experiments described in the previous section give the sensitivities of an uncoupled ocean model driven by prescribed fluxes. We would like to compare this with the concept of the delayed oscillator. To this end we take as a reference trajectory x_i the model climatology (assuming this is in fact a solution of the model equations), and interpret the small deviations δx in the adjoint as anomalies with respect to this monthly climatology. An adjoint experiment with as target function the NINO index N (either NINO3 or NINO3.4) then gives for the contribution of the atmosphere to the index anomaly

$$\delta N^{\text{atm}} \approx \sum_i \frac{\partial N}{\partial \mathcal{F}_i} \cdot \delta \mathcal{F}_i, \quad (21)$$

with i labelling the one-month time steps and $\delta\mathcal{F}_i$ anomalous flux fields; an integral over the area is indicated by the dotproduct. This relationship is not exact: non-linear terms are not included in the adjoint, but certainly play a role with temperature anomalies of a few Kelvin. The non-linear terms will show up as different values of the sensitivities $\partial N/\partial\mathcal{F}$ for different states of the system.

We refer to each term of the sum in Eq. (21) as the *influence* of this month on the target function. With the help of the adjoint of the statistical atmosphere described in section 2.2 this sum can be approximated by

$$\sum_i \frac{\partial N}{\partial\mathcal{F}_i} \cdot \delta\mathcal{F}_i \approx \sum_i \frac{\partial N}{\partial\mathcal{F}_i} \frac{\partial\mathcal{F}_i}{\partial T_i} \cdot \delta T_i, \quad (22)$$

with δT_i the HOPE SST anomaly field. Of course, as the statistical atmosphere was not in fact used in the forward run we have to check that this approximation holds, *i.e.*, that the statistical atmosphere would have given fluxes similar to the ones actually used.

The total anomaly of the NINO index, δN , consists of the atmospheric contribution described above, plus contributions from the derivative to the initial state and the relaxation to the observed SST. The influence of the initial state x_0 can be neglected for integration times longer than about 1.5 years in our model (see Fig. 10). The influence of the relaxation, which was necessary to keep the model close to reality, is of course very artificial and is not considered further.

The next step is to try to factorize these influences into a sensitivity times an anomaly. To this end we use an EOF expansion

$$\begin{aligned} \frac{\partial N}{\partial\mathcal{F}_i} \frac{\partial\mathcal{F}_i}{\partial T_i} \cdot \delta T_i &= \sum_n \frac{\partial N}{\partial\mathcal{F}_i} \frac{\partial\mathcal{F}_i}{\partial T_i} \cdot e_n e_n \cdot \delta T_i \\ &\approx \frac{\partial N}{\partial\mathcal{F}_i} \frac{\partial\mathcal{F}_i}{\partial T_i} \cdot e_1 e_1 \cdot \delta T_i. \end{aligned} \quad (23)$$

The last approximation is that the first EOF (Fig. 1a) explains most of the variability of the NINO index.

Finally, we realize that all indicators of sea temperature in the eastern Pacific are highly correlated, and approximate

$$e_1 \cdot \delta T_i \approx C^{(1)} \delta N_i \quad (24)$$

$$e_1 \cdot \frac{\partial}{\partial T_i} \approx C^{(2)} \sum_{\substack{\text{index} \\ \text{region}}} \frac{\partial}{\partial T_i}. \quad (25)$$

This finally gives the dependence of the index to itself some time earlier

$$\delta N_n = \sum_{i=1}^n a_i(N_n) \delta N_{n-i} , \quad (26)$$

The variation of the coefficients a_i with the conditions in different experiments points to non-linear effects parametrized by cubic terms. This formulation is similar to the finite-difference scheme introduced in the last section of Cane et al. (1990). The time delays inherent in the propagation of Kelvin waves to the eastern Pacific compared to the heat retention scale make a finite difference scheme a more natural choice than a differential form.

5.2 Influence of SST anomalies

We try to follow these steps for the experiments described in section 4. The first step is to study the influences defined in Eq. (21) over two years previous to the measurements. Surprisingly, we find large influences in the extra-tropics, probably due to spurious correlations in the statistical atmosphere model. There are also well-known problems of our HOPE version in the Gulf of Panama. We therefore only take into account the region 20°S to 20°N west of 120°W, and 5°S to 5°N east of this line. It is clear that the NINO3.4 index is further away from the problem regions, so we concentrate on this index (which, incidentally, is also more persistent and easier to predict).

The influences of Eq. (21) are plotted in Fig. 10 for three experiments in 1986–1988. The anomalies were computed as in the statistical atmosphere, relative to a 30-year average of model-generated temperatures. It is clear that, within the restrictions of the model and adjoint model, the influence of temperature anomalies more than one year before the measurement is minimal.

The sums of the influences plotted in Fig. 10 are shown in Table 1. The transition and cold experiments are reproduced fairly well, but it seems that the statistical atmosphere would not have been able to simulate the warm phase correctly. The first EOF explains 60–100% of the influences.

We can conclude that the statistical atmosphere, restricted to the tropical region, does a reasonable job of propagating the sensitivities of the NINO3.4 index to fluxes into sensitivities to SST.

5.3 Sensitivities of the indices to themselves

We now have the influences in the factorizable form of Eq. (23). In order to obtain a description which can be compared to the delayed oscillator

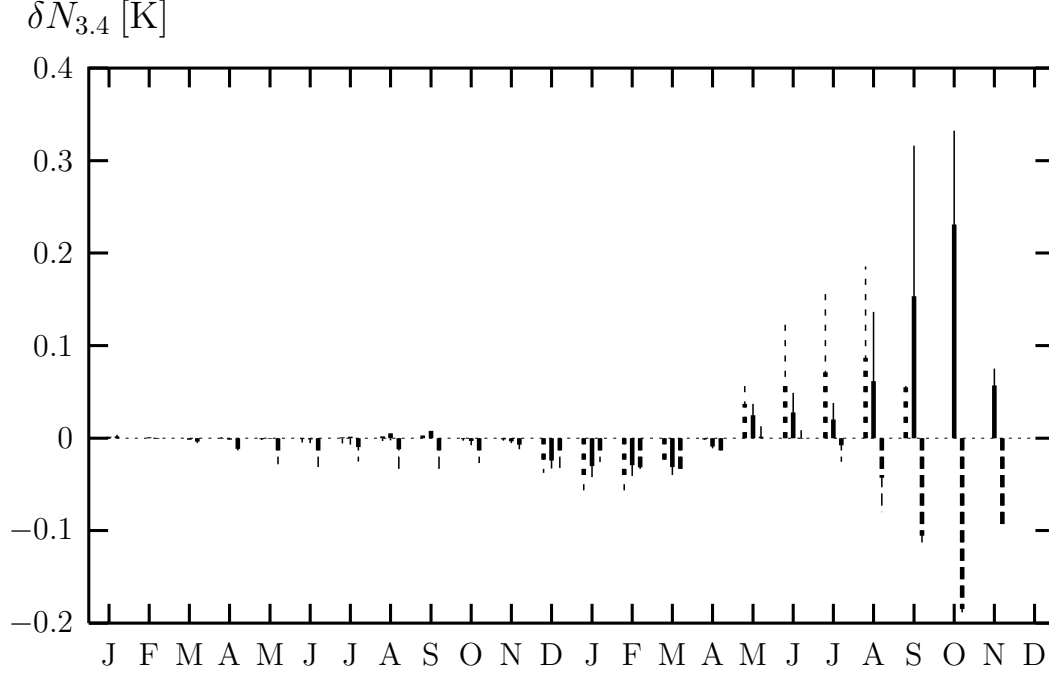


Figure 10: The influence of the SST anomalies on the NINO3.4 indices through the statistical atmosphere at the end of October 1987 (left, dashed), December 1987 (middle, solid line) and December 1988 (right, long dashes). The fraction explained by the first EOF is indicated by the thicker lines.

target index	target date	observed δN^{obs}	simulated δN^{sim}	atmosphere δN^{atm}
NINO3.4	Oct 1987	1.81	2.05	0.36
NINO3.4	Dec 1987	1.07	0.54	0.79
NINO3.4	Dec 1988	-1.94	-1.27	-0.84
NINO3	Oct 1987	1.50	1.97	-0.03
NINO3	Dec 1987	1.02	0.36	0.61
NINO3	Dec 1988	-1.49	-0.56	-0.39

Table 1: Comparison of the NINO3 and NINO3.4 indices as simulated by HOPE with their value deduced from the influences (Fig. 10); for comparison the observed value is also given.

paradigm we convert the sensitivities to the EOF to sensitivities to the indices themselves. Over the 42-year simulation period discussed in section 2.3 we find that $\delta T_i \cdot e_1$ has a correlation of $r = 0.95$ with the NINO3 index, and $r = 0.96$ with the NINO3.4 index; the corresponding constants are $C_3^{(1)} = 0.57$ and $C_{3.4}^{(1)} = 0.51$. The derivatives were fitted over the last 12 months of the six experiments. Except for the final two months, when the adjoint fields are still close to the index region, the agreement is very good, as the adjoint fields are mainly confined to the tropical region. The proportionality constants are $C_3^{(2)} = 2.8$, $C_{3.4}^{(2)} = 4.2$.

Finally, we can study the sensitivity of a NINO index to itself a few months earlier, $\partial N_n / \partial N_i$, which is shown in Fig. 11. The total sensitivity dN_n / dN_i that occurs in the discretized form of the delayed oscillator equation (26) is larger by a factor of about $1.5C^{(1)}C^{(2)}$; this is 2.4 for the NINO3 index, 3.6 for the NINO3.4 index. This scale factor has a rather large uncertainty due to the various approximations made.

As expected, the ‘immediate’ positive feedback differs very much between a situation where the index is falling to zero (Dec 1987) and a situation in which the index is strongly positive (Oct 1987) or negative (Dec 1988). This is the effect of the non-linear effects that are parametrized by the T^3 term in Eq. (1). In cold conditions, the thermocline has disappeared in our model, so that a Kelvin wave in the second baroclinic mode, varying the thermocline depth, is not very effective at changing SST. During a warm episode the thermocline is so deep that the effect of such a wave is also smaller. The effect of a Kelvin wave in the first baroclinic mode is not sensitive to the thermocline depth. The effect of these nonlinearities in the positive feedback is larger for the NINO3 index than for the NINO3.4 index, as the thermocline is shallower in the NINO3 region and hence variations of its depth have a larger effect.

The approximation that the Bjerknes feedback is instantaneous does not seem to be a very good one, especially for the NINO3 index. Part of the delay is due to the artificial 1-month delay of the statistical atmosphere, but another 2–3 months are due to time it takes for a Kelvin wave generated at the date line to reach the signal region. This effect is of course smaller for the NINO3.4 index.

The negative feedback consists of an overlapping train of $n = 1$ Rossby waves that are reflected off different parts of the coast, instead of an idealized peak. Combined with the lower effective group velocity shown in Fig. 4 we obtain negative influences from 6 to about 18 months prior to the measurement. Higher order Rossby waves do not contribute at these timescales. Due to the normalization uncertainties it is difficult to gauge the extend to which

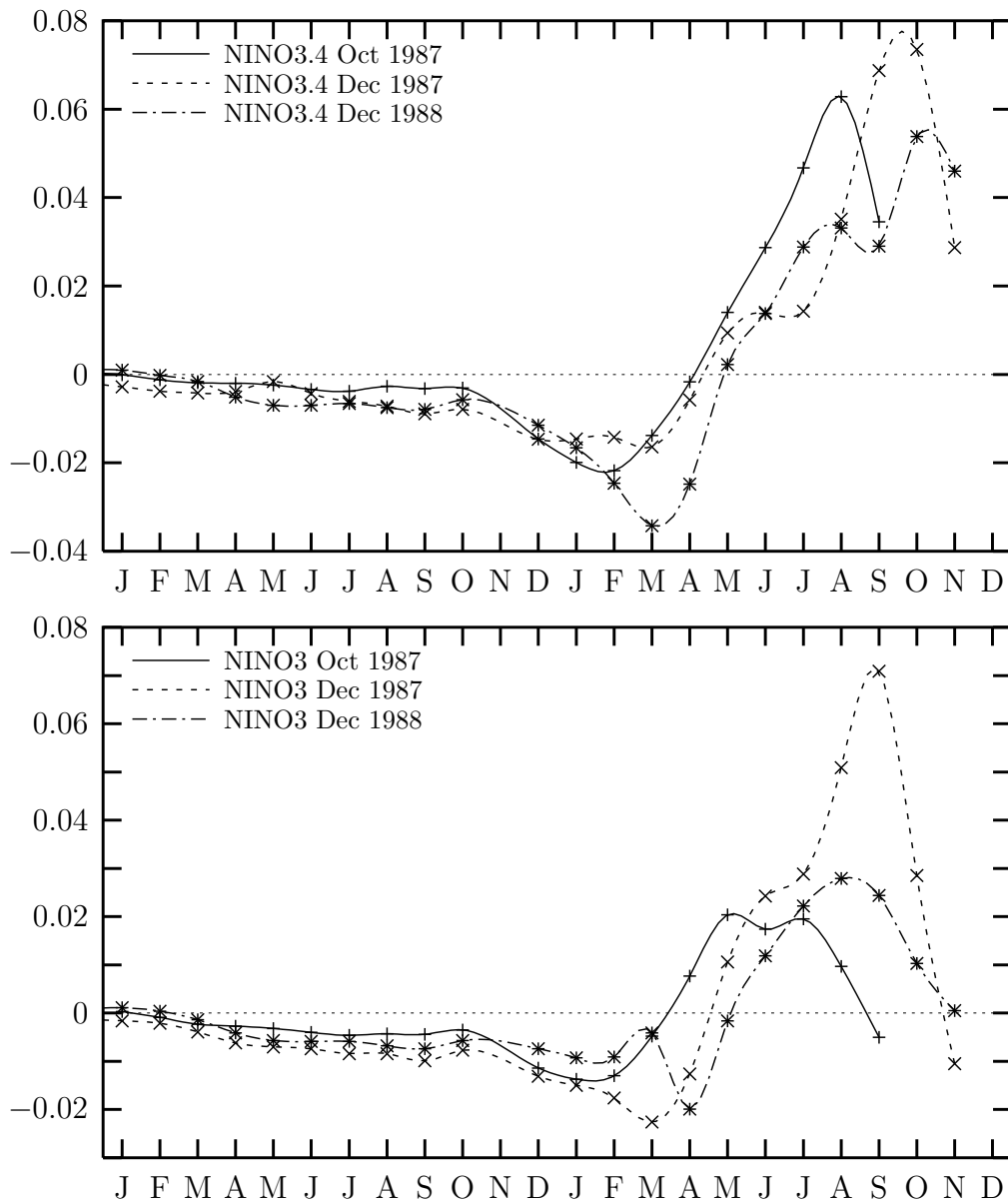


Figure 11: The sensitivity of the NINO3 and NINO3.4 indices to the same index at the end of 1987 and 1988 through the statistical atmosphere in K/K/month. Including the sensitivity to correlated SST changes would roughly result in a factor three increase.

the summed positive feedback exceeds one, and compare this quantitatively with the negative feedback terms (*i.e.*, to determine the parameters in Eq. (1) or Eq. (26) in our model).

However, it is clear from the figure that the negative terms do not depend on the initial state in the same non-linear way as the positive terms. The negative feedback is much stronger than expected for the December 1988 experiments. We suspect that this is due to the non-linear interactions between the different baroclinic modes that we observed in section 4.2. The weak positive response was due to the small amplitude at the surface of the first baroclinic mode adjoint Kelvin wave that is excited. On the other hand, the adjoint Rossby waves that determine the negative feedback propagate in the usual second baroclinic mode in the thermocline, which has a larger amplitude at the surface for the same energy content and is thus more easily excited by a wind anomaly. At the reflection in shallower waters at the western boundary the energy is transferred down from Rossby waves in the second baroclinic mode to Kelvin waves in the deeper first mode.

6 Conclusions

We studied the causes of variations of the sea surface temperature in the eastern equatorial Pacific with an adjoint OGCM and statistical atmosphere. The adjoint gives us first-order estimates of the sensitivity of the NINO3 and NINO3.4 indices of this temperature to forcing fields and state fields some time earlier. We generated these sensitivities at the end of October 1987, December 1987 and December 1988; respectively warm, transition and cold phases of ENSO. In these experiments we used prescribed fluxes to drive the ocean model HOPE.

The sensitivities either damp out exponentially (heat flux, previous SST) with a time scale of about one month, or propagate as equatorial Kelvin and Rossby waves (wind stress, sea level). Of course, without a full atmosphere model we cannot observe small-scale coupled modes.

A change in temperature of the NINO3 region can be effected by a Rossby wave coming from the eastern coast. In our model some of this influence is reflected back — an equatorial Kelvin wave impinging on the eastern coast can generate such a Rossby wave, albeit not very efficiently. Another way the temperature can be changed is by the arrival of a Kelvin wave from the west; these are clearly visible in the sensitivities to the wind stress and sea level. This Kelvin wave can be generated by Rossby waves reflecting off the coast of New Guinea and the Philippines, either directly or with a few months' delay at the western boundary area. These delays, combined

with the eastern reflections, give rise to an effective group velocity of the sensitivities that is lower than the speed of the individual Kelvin and Rossby waves. Higher order adjoint Rossby waves are observed, but do not have a strong enough wind stress sensitivity field to be able to influence the eastern Pacific. These waves sum to a sensitivity to the thermocline depth in the warm pool off the equator, but there is no sensitivity to the zonally-averaged thermocline depth along the equator at long timescales.

The speed of the adjoint Kelvin waves depends very much on the state of the ocean in our model at the measurement region. Note that we do not simulate Kelvin waves as they occur in the ocean, but as they influence the NINO3 index. Normally these propagate in the second baroclinic mode (with a zero at the thermocline), with $c \approx 2 \text{ ms}^{-1}$ in the western and central Pacific. However, in the cold tongue during the cold phase (La Niña), the thermocline is so shallow that the first baroclinic mode is excited, with a speed $c \approx 3 \text{ ms}^{-1}$ in the central Pacific. These different modes mix at the reflection in shallow waters at the west coast; the reflected adjoint Rossby waves have speeds compatible with the second baroclinic modes (the third for higher order Rossby waves). These results should be compared to an observed speed of $2.4 \pm 0.3 \text{ ms}^{-1}$, independent of longitude, from the TOGA-TAO array.

We used an adjoint statistical atmosphere model to convert the sensitivities into fluxes (mainly wind stress) into sensitivities to the SST. This gives a reasonable description of the observed NINO3.4 index anomalies at the three times we did experiments for. Next we compared these influences with the average index anomaly times the average sensitivity in the corresponding region. This underestimates the size of the influence by a factor of roughly four, but does not change the shape as a function of time very much, due to the high correlations of the neglected terms with the included ones.

The resulting response function (Fig. 11) shows the essence of the delayed oscillator mechanism. Going back from the measurement time, the first few months exhibit the positive feedback of the change in trade winds reinforcing the SST anomaly. At about half a year before the target date the feedback changes sign as Rossby waves reflect off the western coast as Kelvin waves with opposite polarity. Both these feedback loops are spread out in time. Kelvin waves are excited most easily in the central Pacific and take about two months to travel to the signal region, and the reflections at the western side occur at different longitudes so that the influence of Rossby waves is spread out over half a year as well.

We also observe that the positive feedback is much stronger when the system is in transition (Dec 1987), than when it is in a warm (Oct 1987) or cold (Dec 1988) phase, pointing to a role of non-linear terms in restraining

the delayed oscillator. We do not observe this effect in the delayed response.

Acknowledgements Geert Jan van Oldenborgh was supported by the Geosciences Foundation (GOA) of the Netherlands Organization of Scientific Research (NWO). We would like to thank Arie Kattenberg, Gerbrand Komen and Femke Vossepoel for many helpful comments on the manuscript.

A Technical details of the adjoint model

Most of the adjoint code was generated by automatic differentiation of the Fortran code of the HOPE and statistical atmosphere models by the (T)AMC (Giering, 1994, 1997). The exceptions were the horizontal and vertical diffusion and viscosity computations in HOPE. These involve the inversion of a tridiagonal matrix, the adjoint of can be written much simpler than the automatically-generated algorithm. We have not checked the code for vectorization as all experiments reported here were performed on a scalar CPU (MIPS R10000).

The adjoint model M^\dagger depends both on the adjoint fields $\partial/\partial x$ and the fields of the reference trajectory x for non-linear functions \mathcal{M} . The latter fields are saved from the forward run of the model to be used in the backward run of the adjoint model in a three-layer scheme. To compute the adjoint of one day (12 ocean time steps), the model is run forward over this period while storing fields needed in non-linear transformations on a direct-access file. Saving these in single precision, and eliminating the multiple storage of the slowly-varying temperature and salinity fields per time step one obtains a 250 MB storage file (21 3D fields of $2^{\circ}97^{\circ}61^{\circ}20$ numbers per time step times 12 steps per day). These daily runs are restarted from restart files generated by a one-month run. Each (modified) restart file takes 8 MB (8 3D fields). The monthly restart files are generated by a top-level run. In all the storage requirements are about 500 MB disk space. The run-time size of the program is 130 MB.

Apart from end effects (the last month can be skipped on the highest level) the running time for an adjoint run is three forward runs (total, month and day) and one backward run. The latter includes many forward recomputations, and takes about 2–3 times longer than a forward run. The total cost of a full adjoint run is therefore 5–6 times the cost of a forward run in CPU time. To this one should add the cost of writing and reading 250 MB temporary storage per simulated day.

We verified whether finite perturbations of the initial state fields did in fact give results in agreement with the adjoint model, which is only strictly

valid for infinitesimal perturbations. For small random perturbations (1–6 wavelengths in x and y and 0–1 in z tapering off with depth) of all initial state variables except temperature and salinity we obtain good agreement with the derivative up to more than 6 months. We did not include variations of the temperature and salinity fields as these give rise to different convection patterns, mainly in the mixed layer at high latitudes. The derivative to the most important input variable, τ_x , is validated more systematically in Appendix B.

B Validation

Although the linear dynamics we found in section 4 looks plausible, it remains to be verified that non-linear effects do not in fact dominate in the model (let alone in Nature). For this purpose we compared the influence of zonal wind fields on the NINO3 index at the end of 1987 with the predictions of the adjoint model, cf. Eq. (12)

$$\delta N_3 \approx \frac{\partial N_3}{\partial \tau_x} \delta \tau_x . \quad (27)$$

All deviations are relative to a forward run with prescribed fluxes⁴. For the extra wind field $\delta \tau_x$ we chose a longitude with a large influence, the size was two grid points at latitude $\pm 1.4^\circ$ with a zonal extent of 20° ; the zonal edges are smoothed over $\pm 5^\circ$. The duration of the storm was matched to the sampling of the derivative fields, 8 days, and its intensity was ± 0.01 and $\pm 0.05 \text{ Nm}^{-2}$, resulting in predicted deviations of the NINO3 index of roughly 0.05 K (1 month) to 0.01 K (1 year) for the higher wind stress.

In Fig. 12 we present the results of these experiments. In the initial adjoint Kelvin wave (Sep–Dec) the ratios almost always are within the range 0.8–1.3. Smaller wind fields give better results, as the error is dominated by non-linear effects. The exceptions are in September, when the reflected Rossby waves influence the picture. The previous two months (Jul–Aug), when the reflections are building up and the perturbations are near the western coast, the adjoint performs poorly. For higher wind fields the ration lies between 0.2 and 2. These perturbations send waves of both signs across the Pacific, so the final perturbation of the NINO3 index is a sum of positive and negative patches that is very sensitive to details.

The situation improves when the adjoint Rossby waves are clearly established (Jan–Jun). When the signal is not too weak the prediction for the

⁴Due to an oversight, relaxed to climatology rather than observed SST; this should not influence the findings.

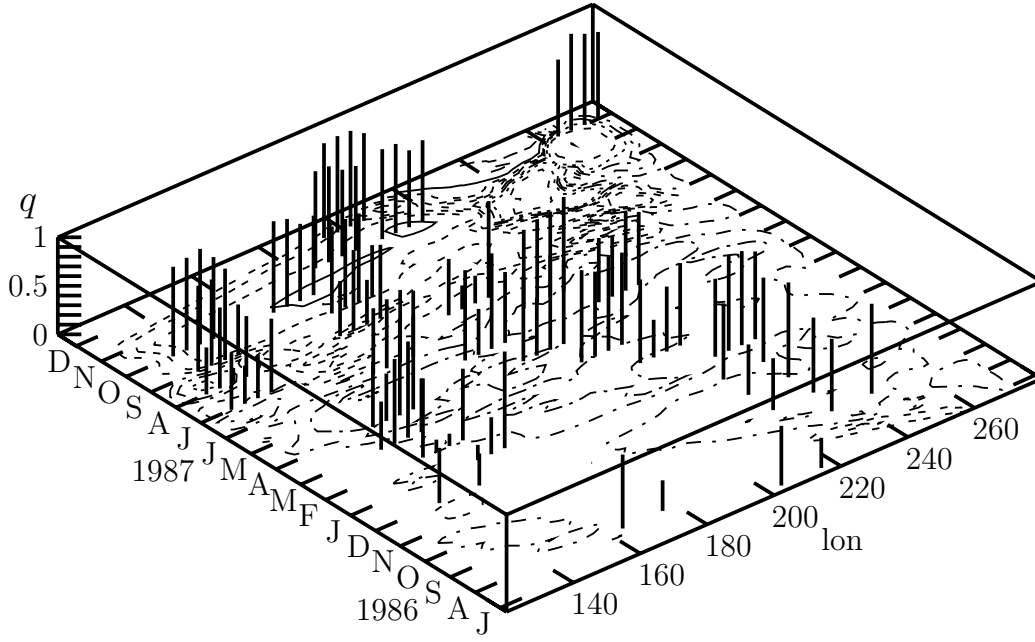


Figure 12: The quality of the adjoint model 1986–1987 run compared with perturbed forward runs. The contour plot is the sensitivity to the zonal wind field, $\partial N_3/\partial \tau_x$. The four bars represent the quality with $\delta \tau_x = -0.05, -0.01, +0.01, +0.05 \text{ Nm}^{-2}$ respectively; the position indicates the longitude and date of the perturbation. The quality is defined as $q = 1 - 2/\pi \arctan |1 - \delta N_3/(\delta \tau_x \partial N_3/\partial \tau_x)|$. It is 1 for perfect agreement, 0.6 when the ratio is 0.5 or 1.5, and it tends to zero for very bad agreement

stronger winds is accurate to within a factor 0.4–1.6 (it tends to be a bit too low). The error is dominated by noise, so that the lower wind fields give worse results. In the previous year we only investigated the stronger wind fields. One sees the same pattern: the well-defined first Rossby wave gives reasonable agreement (although the derivative again underestimates the real effect by a factor 1.5 on average). However, the effect of a wind field outside the strongest wave is predicted poorly by the adjoint.

Date	longitude	$\delta\tau_x$ [Nm ⁻²]	δNINO3 [K]	adjoint [K]	ratio
Oct 1987	160°–180°	0.2	0.295	0.199	1.48
		–0.2	–0.173	–0.199	0.86
Jun 1987	160°–180°	0.2	–0.041	–0.069	0.60
		–0.2	0.062	0.069	0.90
Jan 1987	225°–245°	0.2	–0.048	–0.048	1.00
		–0.2	0.060	0.048	1.25
Aug 1986	160°–180°	0.2	0.000	–0.019	–0.02
		–0.2	0.012	0.019	0.64

Table 2: The effect of 8-day stronger anomalous wind bursts over 20°×4° along the equator.

We also studied the effect of stronger anomalous wind stress fields, $\delta\tau_x = 0.2 \text{ Nm}^{-2}$, which is the typical strength of a westerly wind burst (Giese and Harrison, 1990). The results are presented in Table 2. Non-linear effects worsen the agreement at short lead times compared to more gentle perturbations, but at longer lead times the results are comparable.

In all, it seems we can trust the sensitivities of the adjoint model most of the time to within a factor 2, even to one year back. This does not hold when the expected deviation is small, or when the perturbation is near the western coasts so that reflected and direct waves interfere.

References

- A. Arakawa and V.R. Lamb. Computational design of the basic dynamical process of the UCLA general circulation model. *Meth. Comput. Phys.*, 17: 173–265, 1977.
- T.P. Barnett, M. Latif, N. Graham, M. Flügel, S. Pazan, and W. White. ENSO and ENSO-related predictability. Part I: Prediction of equatorial

- Pacific sea surface temperature with a hybrid coupled ocean-atmosphere model. *J. Climate*, 6(8):1545–1566, 1993.
- A. G. Barnston and C. F. Ropelewski. Prediction of ENSO episodes using canonical correlation analysis. *J. Climate*, 7:1513–1564, 1992.
- D. S. Battisti and A. C. Hirst. Interannual variability in a tropical atmosphere-ocean model: influence of the basic state, ocean geometry and nonlinearity. *J. Atmos. Sci.*, 46:1687–1712, 1989.
- J. Bjerknes. A possible response of the atmospheric Hadley circulation to equatorial anomalies of ocean temperature. *Tellus*, 18:820–829, 1966.
- J.-P. Boulanger and L.-L. Fu. Evidence of boundary reflection of Kelvin and first-mode Rossby waves from TOPEX/POSEIDON sea level data. *J. Geophys. Res.*, 101(C7):16361–16371, 1996.
- J.-P. Boulanger and C. Menkes. Propagation and reflection of long equatorial waves in the Pacific ocean during the 1992–1993 El Niño. *J. Geophys. Res.*, 100(C12):25041–25059, 1995.
- G. Burgers. The El Niño stochastic oscillator. *submitted to J. Climate*, 1997. e-print physics/9706007.
- M. A. Cane, M. Munnich, and S. E. Zebiak. A study of self-excited oscillations of the tropical ocean-atmosphere system. Part I: linear analysis. *J. Atmos. Sci.*, 47:1562–1577, 1990.
- Y. Chao and S. G. H. Philander. On the structure of the Southern Oscillation. *J. Climate*, 6:450–469, 1993.
- D. B. Chelton and M. G. Schlax. Global observations of oceanic Rossby waves. *Science*, 272:234–238, 1996.
- DKRZ. The ECHAM 3 atmospheric general circulation model. Technical Report No. 6, Deutsches Klimarechenzentrum, Bundesstr. 55, 20146 Hamburg, Germany, 1992.
- R. Giering. *Adjoint Model Compiler*. Max-Planck-Institut für Meteorologie, Hamburg, 1994. Available at <http://klima47.dkrz.de/giering/amc>.
- R. Giering. *Tangent linear and Adjoint Model Compiler, Users manual*. Max-Planck-Institut für Meteorologie, Hamburg, 1997. Available at <http://klima47.dkrz.de/giering/amc>.

- R. Giering and T. Kaminski. Recipes for adjoint code construction. *ACM Trans. Math. Software*, to appear, 1996. Max-Planck-Institut für Meteorologie Report no. 212.
- B. S. Giese and D. E. Harrison. Aspects of the Kelvin wave response to episodic wind forcing. *J. Geophys. Res.*, 95(C5):7289–7312, 1990.
- A. E. Gill. *Atmosphere-Ocean Dynamics*. Academic Press, Orlando, 1982.
- M. Ji, A. Leetmaa, and V. E. Kousky. Coupled model predictions of ENSO during the 1980s and 1990s at the National Centers for Environmental Prediction. *J. Clim.*, 9:3105–3120, 1996.
- F.-F. Jin. An equatorial recharge paradigm for ENSO, part I. *J. Atmos. Sci.*, 54:811–829, 1997.
- W. S. Kessler and M. J. McPhaden. Oceanic equatorial waves and the 1991–93 El Niño. *J. Climate*, 8:1757–1774, 1995.
- W. S. Kessler, M. J. McPhaden, and K. M. Weickman. Forcing of intraseasonal Kelvin waves in the equatorial Pacific. *J. Geophys. Res.*, 100(C6):10613–10631, 1995.
- R. Kleeman, A. Moore, and N. R. Smith. Assimilation of subsurface thermal data into a simple ocean model for the initialization of an intermediate tropical coupled ocean-atmosphere forecast model. *Mon. Wea. Rev.*, 123:3103–3114, 1995.
- M. Latif, T. Stockdale, J.O. Wolff, G. Burgers, E. Maier-Reimer, M.M. Junge, K. Arpe, and L. Bengtsson. Climatology and variability in the ECHO coupled GCM. *Tellus*, 46A:351–366, 1994.
- S. Levitus. Climatological atlas of the World Ocean. *US Department of Commerce, NOAA Prof Pap 13*, 1982.
- N. J. Mantua and D. S. Battisti. Evidence for the delayed oscillator mechanism for ENSO: the “observed” Kelvin mode in the far western pacific. *J. Phys. Oceanogr.*, 24:691–699, 1994.
- J. D. Neelin. The slow sea-surface temperature mode and the fast-wave limit: Analytic theory for tropical interannual oscillations and experiments in a hybrid coupled model. *J. Atmos. Sci.*, 48:584–606, 1991.

- D. E. Parker, C. K. Folland, A. Bevan, M. N. Ward, M. Jackson, and K. Maskell. Marine surface data for analysis of climatic fluctuations of interannual to century timescales. In Martinson D. G., K. Bryan, M. Ghil, M. M. Hall, T. R. Karl, E. S. Sarachik, S. Soroostian, and L. F. Talley, editors, *Natural Climate Variability on Decade-to-Century Time Scales*, pages 241–250, 222–228. National Academy Press, 1994.
- C.A. Paulson and J.J. Simpson. Irradiance measurements in the upper ocean. *J. Phys. Oceanogr.*, 7:952–956, 1977.
- S. G. Philander. *El Niño, La Niña and the Southern Oscillation*. Academic Press, San Diego, 1990. 293 pp.
- R. W. Reynolds and T. M. Smith. Improved global sea surface analyses using optimum interpolation. *J. Clim.*, 7:929–948, 1994. The NINO index data are available at <http://nic.fb4.noaa.gov/data/cddb/altindex.html>. Note that the NINO3.4 indices changed recently.
- E. Roeckner, K. Arpe, L. Bengtsson, L. Dümenil, M. Esch, E. Kirk, F. Lunkeit, M. Ponater, B. Rockel, R. Sausen, U. Schlese, S. Schubert, and M. Windelband. Simulation of the present day climate with the ECHAM model: Impact of model physics and resolution. *Report No. 93*, 1992. (Available from Max-Planck-Institut fuer Meteorologie, Bundesstr. 55, 20146 Hamburg, Germany).
- N. Schneider, T.P. Barnett, M. Latif, and T. Stockdale. Warm pool physics in a coupled GCM. *J. Climate*, 9:219–239, 1996.
- P. S. Schopf and M. J. Suarez. Vacillations in a coupled ocean-atmosphere model. *J. Atmos. Sci.*, 45:549–566, 1988.
- M. J. Suarez and P. S. Schopf. A delayed action oscillator for ENSO. *J. Atmos. Sci.*, 45:3283–3287, 1988.
- G. T. Walker. Correlation in seasonal variations of weather VIII, IX. *Mem. Indian Meteorol. Dep.*, 24:75–131, 275–332, 1923, 1924.
- J.-O. Wolff, E. Maier-Reimer, and S. Legutke. The Hamburg Ocean Primitive Equation model HOPE. Technical Report No. 13, Deutsches Klimarechenzentrum, Bundesstr. 55, D-20146 Hamburg, Germany, Hamburg, 1997.
- K. Wyrtki. El Niño — the dynamic response of the equatorial Pacific ocean to atmospheric forcing. *J. Phys. Oceanography*, 5:572–584, 1975.

S. E. Zebiak and M. A. Cane. A model of El Niño–Southern Oscillation.
Mon. Wea. Rev., 115:2262–2278, 1987.